Liver regeneration by oval cells employing bistability of stemness-senescence, Hippo signaling, EMT-MET, and polyploidy circuit

Marija Lazovska[1,3] *, Kristine Salmina[3], Dace Pjanova[2,3], Bogdan I. Gerashchenko[4] and Jekaterina Erenpreisa[3]

[1] Institute of Oncology and Molecular Genetics, Riga Stradins University, Riga, Latvia

[2] Riga Stradins University, Riga, Latvia

[3] Latvian Biomedical Research and Study Centre, Riga, Latvia

[3] R.E. Kavetsky Institute of Experimental Pathology, Oncology and Radiobiology, National Academy of Sciences of Ukraine, Kyiv, Ukraine; biger63@yahoo.com

* Corresponding author

Email: marija.lazovska@rsu.lv (ML)

Abstract

Liver hepatocytes possess remarkable regenerative capabilities, yet severe damage may compromise this process. Liver progenitor ("oval") cells exhibit the potential to differentiate into both hepatocytes and cholangiocytes, making them promising candidates for cell therapy. However, their mechanisms in liver regeneration are not clear. Here, on rat liver oval stem-like epithelial cells (WB-F344) a wound healing assay was performed. The scratched near-confluent monolayers (70% area removed) underwent the G1-arrest, bi-nucleation at 10-12 hours post-wounding, starting movement of epithelial to mesenchymal transition (EMT) cell portion into the wounded areas. Nanog nuclear upregulation, fragmentation, and transition as granules into cytoplasm and around, along with $p16^{Ink4a}$ nuclear intrusion from the cytoplasm, loss of epithelial markers, and YAP1/Hippo activation were seen near the wound edge. The replicative stress and proliferation boost followed, documented at 24 hours. Proliferation concluded at 40-48 hours, accomplished by reconstitution of epithelial tissue, the disappearance of Nanog granulation and $p16^{Ink4a}$ return to the cytoplasm, releasing excess. This investigation reveals novel regulatory facets in liver regeneration by oval cells. It accentuates the stemness-senescence bistable switch regulated by reciprocal nucleo-cytoplasmic transitions of opposite regulators, coordinated with Hippo-pathway switch, replicative stress, and boost, along with ploidy, EMT-MET and paracrine secretome circuits - enabling successfully resolving the massive injury.

Keywords: liver regeneration; oval cells; bipotential progenitor; stemness-senescence; EMT-MET; polyploidy circuit; turbulence; replication stress; Hippo pathway.

Fig 1. Graphical abstract. Bistable nuclear-cytoplasmic switch between stemness and senescence regulators in the wound healing process by oval liver cells: (1-2) Priming phase: (1) at the wound edge,

36 (2) in the wound; (3) Proliferative phase, wound closure. Nanog – green; p16INK4A – red, EMT cell -

37 with blue nucleus.

Introduction

The mammalian liver possesses a remarkable capacity to regenerate after the injury while recovering its volume and functionality. However, the regenerative capacity of the liver is not endless: while the removal of up to two-thirds of the liver (partial hepatectomy; PH) introduced in the experiment by Higgins and Anderson in 1931 [1] can be safely repaired, larger resection is at risk of liver failure and following the death of the patient. Unfortunately, there could be life-threatening situations due to progressive complications of liver pathology that need to be eradicated as soon as possible by surgical means. According to statistics, hepatic disease is one of the top causes of death globally and there is an ascending tendency of diseases such as Hepatitis B and C often ending in cirrhosis and liver cancer [2]. At present, stem cell therapy is being extensively explored to tackle prognostically unfavorable liver diseases [3]. Despite the progress, the challenges remain, and yet liver transplantation remains the only curative treatment for patients with end-stage liver diseases.

Liver progenitor cells (LPCs)-driven liver regeneration was shown to be activated in case of massive liver injuries (Duncan et al., 2009). It involves the activation and proliferation of the LPCs expressing developmental markers and having the potential to become both mature hepatocytes and biliary cells [4]. The events induced after the typical liver injury are usually categorized into three phases: priming (activation), proliferation and termination [5]. Different signaling pathways and molecular processes are involved, both LPCs- and hepatocyte-driven, also called typical liver regeneration performed by a healthy liver. Many pathways are shared by both types of regeneration, but LPCs-driven repair remains less understood. The Hippo pathway, one of the central growth regulators, was shown to accompany the whole healing process from cell activation to the termination of response [6]. This pathway is involved in replicative stress [7], and cellular polyploidy, which is described in normal liver and boosted by

regeneration [8, 9]. Senescence is another mechanism involved in liver repair; however, its role is controversial and poorly understood [10, 11]. The unique hepatocyte plasticity and reprogramming to an early postnatal-like state in response to injury were shown using a single-cell RNA sequencing [12].

In this work, using an *in vitro* wound healing assay, we study rat LPCs (known as "oval" epithelial cells) in response to mechanical injury. The primary goal of the study is to find out how the previously described mechanisms are interconnected in time and space by combining phenotypical and molecular studies of LPCs throughout the healing process. Here, in addition to the already known "polyploidy circuit", in which polyploid hepatocytes undergo ploidy reduction during injury response and subsequent re-polyploidization [13] together with Hippo pathway on-off state, we describe cooperation and "competition" between the opposite regulators of cell fate - senescence/quiescence and stemness/self-renewal. Replicative stress, which is likely imposed by YAP1 in this wound healing assay, could be a key contributor in this bistability directed towards the regulation of cell-fate changes.

Methods

The cell line

The non-transformed male diploid WB-F344 rat liver epithelial cell line [14] was kindly provided by Dr. Tomonori Hayashi (Radiation Effects Research Foundation, Hiroshima, Japan). It is a benign wild-type p53 stem-like cell line, rapidly proliferating, and potentially capable of differentiating into both hepatocytes and cholangiocytes. In addition, these cells are relatively radioresistant as they do not undergo rapid and massive cell death even after high-dose irradiation up to 10 Gy [15]. The cells were cultured in RPMI 1640 growth medium (Sigma-Aldrich, St. Louis, MO, USA) supplemented with 7% fetal bovine serum (FBS) (Sigma-Aldrich, St. Louis, MO, USA) and 600 μg/ml L-glutamine (Gibco; Thermo Fisher Scientific, Waltham, MA, USA). Cells were incubated at 37°C in a humidified 5% CO2 atmosphere with

82 complete medium replacement performed every 24 h. Cells were routinely subcultured after reaching 70-
83 80% confluency every three days.

84 Wound healing (scratch) assay

85 Before wound healing assay, cells were grown on 4-well glass chamber slides coated with poly-D-lysine
86 (Thermo Fisher Scientific, Waltham, MA, USA). About 70,000 cells were seeded in each chamber well
87 with a total aliquot of growth medium of 1 ml. To mimic the organ regeneration after the wounding and
88 to test the wound-induced plasticity of WB-F344 cells, a simple wound healing (scratch) assay was
89 applied. For this purpose, cell monolayers that were maintained in chamber slides reaching the near-
90 confluence of approximately 95% after 24–30 h culturing were used. A sterile 1000 µl pipette tip was used
91 to scratch a grid composed of longitudinal and transverse lines (approximately 9 and 6 lines, respectively),
92 so the distance between the closest non-intersecting lines was almost equal (~ 2 mm). Approximately two-
93 thirds of the monolayer was removed. To take away cell debris, the cell monolayers were washed three
94 times with pre-warmed culture media by gentle shaking followed by the addition of fresh media. Cells
95 were then incubated at the aforementioned conditions until the desired time point or full closure of the
96 wound. An Experimental design of the wound healing assay is shown in Fig 2.

97 **Fig 2. Experimental design.** Monolayers of WB-F344 cells after reaching near 100% confluence in
98 chamber slides were scratched and at 40, 24, and 12 h after wounding were fixed and stained with
99 Toluidine blue (TB) for analysis. The highlighted enlarged region of interest from one of the TB-stained
100 monolayers demonstrates different densities of cells in damaged (scratched) and non-damaged (non-
101 scratched) areas colored in white and blue, respectively. Based on spatial localization to wound the edge
102 the cells were subsequently analyzed for DNA content by image cytometry and cell-cycle phase-
103 dependent nuclear morphology.

Immunofluorescence staining

For immunofluorescence staining the chamber slides with live scratched adherent cells were removed from growth media and rinsed three times with warm phosphate-buffered saline (PBS), pH=7.4 (Sigma-Aldrich, St. Louis, MO, USA), and afterwards a droplet of warm FBS was added to each well. Before the next manipulations, a chamber was gently pulled off from the slide and the slides were allowed to shortly air-dry vertically. Then cells were fixed in methanol for 7 min at -200C, dipped 10 times in ice-cold acetone, and allowed to briefly dry. Slides were washed three times in 0.01% tris-buffered saline/Tween 20 (TBST) for 5 min each. Subsequently, they were blocked for 40 min in 1% bovine serum albumin (BSA) in PBS with 0.05% Tween-20 (Sigma-Aldrich, St. Louis, MO, USA) at room temperature (RT). After blocking, the samples were covered with 1% BSA in PBS with 0.025% Tween-20 containing primary antibodies and incubated overnight at 40°C in a humidified chamber. The next day, slides were washed five times in 0.01% TBST and covered with TBST containing appropriate secondary antibody in 1:300 dilution (goat anti-mouse IgG Alexa Fluor 488, goat anti-rabbit IgG Alexa Fluor 594 (Invitrogen, Carlsbad, CA, USA)) and incubated for 40 min at RT in the dark in a humidified chamber. After incubation, the samples were washed again five times with 0.01% TBST and once for 2 min in 1xPBS. Cells were counterstained with DAPI (0.25 μg/ml) for 2 min and embedded in Prolong Gold (Invitrogen, Carlsbad, CA, USA). When staining for α-tubulin and actin, the cells were fixed with fresh warm (~ 37°C) 4% paraformaldehyde for 15 min at RT, then washed three times with 1xPBS and permeabilized with 0.5 % Triton-X100 (Sigma-Aldrich, St. Louis, MO, USA) in 1xPBS for another 5 min, washed again; and further the previously described steps starting from blocking were carried out. Three independent experiments for each combination of primary antibodies were performed. For microscopic observations and sample analysis, a fluorescent light microscope (Leitz Ergolux L03-10, Leica, Wetzlar, Germany)

126 equipped with a color video camera (Sony DXC 390P, Sony, Tokyo, Japan) and RGB filter-set were used.

127 Primary antibodies and their sources are listed in Table 1.

128 **Table 1. List of antibodies used in this study for immunofluorescence staining.**

Antibody Against	Description	Used concentration	Product no. and Manufacturer
α-Tubulin	Mouse monoclonal	1:200	T5168, Sigma-Aldrich, St. Louis, MO, USA
Albumin	Rabbit polyclonal	1:200	PA5-85166, Invitrogen, Carlsbad, CA, USA
Nanog	Mouse monoclonal	1:50	N3038, Sigma-Aldrich, St. Louis, MO, USA
Twist1	Mouse monoclonal	1:100	sc-81417, Santa Cruz, Dallas, TX, USA
Cytokeratin 7	Mouse monoclonal	1:100	MA1-06315. Invitrogen, Carlsbad, CA, USA
Oct 3/4	Mouse monoclonal	1:40	sc-5279, Santa Cruz, Dallas, TX, USA
p16^{Ink4a}	Rabbit polyclonal	1:50	ab84075, Abcam, Cambridge, UK
TEAD1	Mouse monoclonal	1:200	GT13112, Invitrogen, Carlsbad, CA, USA
F-ACTIN	Phalloidin-iFlour 594 Conjugate	1:300	ab176757,

			Abcam, Cambridge, UK
YAP1	Rabbit polyclonal	1:500	PA-46189, Invitrogen, Carlsbad, CA, USA
c-Myc	Mouse monoclonal	1:100	sc-40, Santa Cruz, Dallas, TX, USA

129 # DNA staining and image cytometry

130 To evaluate DNA amount in cells, count mitotic figures and estimate cell cycle dynamics the samples
131 were stained with toluidine blue (TB) by the method [16], by the following protocol. Chamber slides with
132 adherent scratched or control cells were washed three times with 1xPBS as described before, with
133 subsequent addition of warm FBS and air-drying for 30 min. Then slides were fixed in ethanol/acetone
134 (1:1) for at least 30 min at 40°C and then air-dried again. Next, slides were hydrolyzed with 5 N HCl for
135 20 min at 20-21°C. In some experiments, to partly preserve RNA staining and observe nuclei together
136 with the cytoplasm, a shortened hydrolysis for 10 sec was performed. Slides were then washed in distilled
137 water five times 1 min each and stained with 0.05% TB in 50% citrate-phosphate McIlvain buffer at pH=4
138 for 10 min. They were briefly rinsed in distilled water and blotted with filter paper. Subsequently, the
139 slides were dehydrated by incubating twice in butanol for 3 min each at 37°C, cleared twice in xylene for
140 3 min each at RT and embedded in DPX. Ready samples were imaged in the green channel using a Sony
141 DXC 390P color-calibrated video camera (Sony, Tokyo, Japan). From the greyscale images, DNA content
142 was measured as the IOD using Image-Pro Plus 4.1 software (Media Cybernetics, Rockville, MD, USA).
143 Cell DNA content or ploidy number was compared to IOD values for metaphases and anaphase-telophase
144 (ratio= 2) and equated to diploid (2C) DNA values in G1 cells. A sum error of 10% was established for
145 this DNA stoichiometry method using in situ image analysis, and this interval was considered for

146 estimating proportional distribution of cell-cycle phases. For cell cycle measurements, approximately 300-
147 500 interphase cells were collected at each experimental time point. Mitotic indexes were measured
148 microscopically per 1000 cells, as well as other characteristics, such as the number of binuclear cells.

149 Statistical analysis

150 Statistical analysis was performed with the Student's t-test tool on Microsoft Office Excel (version 2401).
151 Statistical significance was assessed at a p-value < 0.05.

152 Results

153 Cell growth arrest and polyploidy/cell cycle changes at the wound edge – 154 the early response

155 In control cells, the cell cycle exhibited a standard distribution, with most cells progressing smoothly
156 through the G1 phase (diploid fraction) (Fig 3B and 3E). G2 and S phases were well-represented,
157 indicating normal cell cycle progression. Upon injury, a notable shift occurred in cell cycle dynamics at
158 12 hours post-injury (hpi). Most cells exhibited arrest at the G1 phase, accompanied by a reduction in G2
159 and S phases, in stark contrast to the control (Fig 3B). Interestingly, the mononuclear polyploid cell (>4C)
160 fraction significantly decreased from 3.88% to 0.95% (Fig 3E and 3F), while the proportion of binuclear
161 cells tripled from 1% to 3%, with a higher accumulation at the wound edges (about 5%) (Fig 3D). This
162 indicated the activation of a polyploidy circuit in response to the wound. Concomitant with considerable
163 G1 phase arrest, the proportion of mitotic cells decreased twofold compared to control (from 1.45% to
164 0.65%) (Fig 3A) at the wound edge. At the same time, there was a fourfold increase in the
165 anaphase+telophase/metaphase ratio (from 1.3 to 5.2) (Fig 3C), highlighting a substantial acceleration of

166 divisions in some small proportion of cells. This early response within the first 12 hours post-injury
167 suggests a complex interplay of cell cycle regulation in reaction to tissue damage.

168 **Fig 3. Post-wounding effects on nuclear morphology quantitative data (A-D), DNA content profiles**
169 **(E-H) and immunofluorescence characteristics of α-tubulin (I) and Twist1 (J) of WB-F344 cells.** (A)
170 Mitotic indexes at different time points after wounding were separately counted within scratched and non-
171 scratched areas. (B) Distributions of mitosis stages of cells at the edge of the wound at different time
172 points after wounding. (C) Distributions of cell-cycle phases (G1, S, and G2) of cells at the edge of the
173 wound at different time points after wounding. (D) Fraction of binucleated cells at the edge of the wound
174 at different time points after wounding. Data presented as a mean ± SE from three independent
175 experiments. ****: $p \leq 0.0001$, ***: $p \leq 0.001$; **: $p \leq 0.01$, *: $p \leq 0.05$, ns: $p > 0.05$. Representative cell-
176 cycle phase distributions by in situ DNA cytometry in control (E) and within the wound edge/gap at 12 h
177 (F), 24 h (G) and 40 h (H) after wounding. The integral optical density (IOD) values shown in arbitrary
178 units correspond to the positioning of DNA content per cell nucleus. The dashed lines represent borders
179 separating cell nuclei exceeding 4C DNA ploidy whose percentages are shown in green. (I) Cells at the
180 wound edge stained for α-tubulin (green) and DNA by DAPI (blue) display two tetraploid daughter cells
181 ("a" and "b") whose centrosomes (shown by black asterisks) are still joined by a long bridge (shown by
182 white solid arrowhead), which is indicative of the relatively recent cytokinesis that took place a few hours
183 ago; however, the daughter cell "b" has already managed to perform an apparent karyokinesis, thus
184 forming a binuclear (2C+2C) cell, whereas the daughter cell "a" remains quiescent. (J) There is no Twist1
185 expression in control (intact cells) with a typical "cobblestone" epithelial pattern of actin staining (red),
186 whereas Twist1 (green) is highly expressed in cell nuclei within the wound edge especially at 12 h after
187 wounding. Here the wound gap is shown by asterisks, and at the wound edge some cells with reorganized

188 actin cytoskeleton have extending lamellipodia (shown by arrowhead). Scale bars = 10 µm (I) and 30 µm
189 (J).

190 Interplay of the opposite senescence and stemness regulators at the early 191 priming phase

192 In the absence of injury, control cells displayed a low-level presence of the senescence marker and Cdk4/6
193 inhibitor $p16^{Ink4a}$ in cell-nuclei and cytoplasm, suggesting some intrinsic balanced activity (Fig 4A).
194 Concomitantly, the stemness regulator Nanog exhibited a moderate nuclear presence in control cells (Fig
195 4A). This baseline expression of Nanog in the absence of injury underscores its role as a master regulator
196 of stemness in oval cells even under normal conditions. Upon initiation of the early priming phase
197 following injury, both $p16^{Ink4a}$ and Nanog displayed increased presence in cell nuclei, as evidenced by
198 comparative immunofluorescence images. Moreover, while in control of confluent cultures a few Nanog
199 granules were encountered in the cytoplasm, their abundance appeared in the cytoplasm and interspersed
200 among cells at the wounded edge at 10-12h (Fig 4B). Interestingly, cells rich in cytoplasmic Nanog
201 granules exhibited weaker nuclear staining for Nanog but stronger staining for $p16^{Ink4a}$ compared to cells
202 with fewer cytoplasmic granules (Fig 4B, arrowed). This observation hints at the dynamic interplay
203 between these regulators and the potential influence of their subcellular localization on the cell's fate.
204 Another stemness and stress-related transcription factor and an immediate early gene response in liver
205 regeneration, Myc was also of interest. While mostly background cytoplasm Myc-staining was seen in
206 control WB-F344 cells (Fig 4E), at 12 hpi, at the wound edge cells, this was particularly concentrated at
207 the centrosome area and outlined the cytoskeleton (Fig 4F), likely being presented by MycN. Its
208 overexpression is known as arresting the centrosome cycle after DNA damage, in cooperation with wild
209 type p53 [17]. However, the absence of Myc in cell nuclei testified to its suppressed activity as a

210 transcription factor, in line with the decreased nuclear location of Nanog when overcompeted by
211 cytoplasmic-nuclear p16^{Ink4a} influx. At the same time, this resulted in the Nanog protein displacement into
212 cytoplasm as granules and conditioning of the microenvironment at a wounded edge with the stemness-
213 self-renewal factor, which could paracrinally and autocrinally boost the next, proliferating phase of wound
214 healing.

215 **Fig 4. Post-wounding effects on localization, expression, and dimensional characteristics of**
216 **immunofluorescence of Nanog and p16^{Ink4a} (A-D), Myc counterstained with DAPI (E-F), TEAD1**
217 **and YAP1 counterstained with DAPI (I-L), and CK7 and albumin counterstained with DAPI (M-**
218 **P**). Notably, at 12 h after wounding, there is an increase of Nanog cytoplasmic granules (size and numbers)
219 accompanied by an increase of p16^{Ink14a} nuclear expression, as the white arrowheads show some most
220 representative cases (B). In contrast, at 40 h after wounding, many variously sized 16^{Ink4a} granules
221 drastically appear in the cytoplasm with the disappearance of Nanog cytoplasmic granules (D). At the
222 same time, Myc at 12 h after wounding (F), compared with the control (E) increases in the cytoplasm,
223 especially in the centrosome area (white arrowhead) of cells located closer to the wound edge. Also, at
224 the wound edge, cells have an increased cytoplasmic Oct4 (H), compared to the control cells that express
225 Oct4 in cytoplasm as well as in nuclei to an insignificant extent representing background levels (G).
226 Differently localized YAP1 and TEAD1 are well expressed over an active wound healing process (J and
227 K), pointing out the fact that after wounding (especially at 12 h; J) TEAD1 becomes markedly expressed
228 in nuclei and cytoplasm of edge cells, and these cells are also characterized by an elevated and distinct
229 nuclear YAP1 expression. However, these peculiarities diminish upon the wound closure time (L).
230 Contrary to cells actively involved in wound healing, control cells have well-defined nucleo-cytoplasmic
231 TEAD1 rings and dimly stained nuclear YAP1 (I). Albumin and CK7 drastically and synchronously
232 change throughout wound healing (N, O, and P). Although there is an apparent difference in their

233 localization, some shared patterns of colocalization may also be present. Further explanations are in the
234 text. Asterisks (*) indicate the wound gap. Scale bars = 30 μm.

235 The change in cell ploidy and fate, motivated us to look at the Hippo pathway, an important cell and tissue
236 growth regulator, in particular its main operators – transcription regulator YAP1 and its binding target in
237 the nucleus, transcription factor TEAD1. Under basal conditions, control cells displayed YAP1 and
238 TEAD1 subdued intensity and were notably absent in nuclei, as depicted in Fig 4I. Interestingly, TEAD1
239 revealed ring-like structures at the inner perimeter of the nuclear envelope (Fig 4I), potentially signifying
240 lamin B1 rotation associated with accelerated cell senescence, which may be an indirect sign of the lamin
241 B1 rotation in accelerated cell senescence and of cell nucleus turbulence observed preceding YAP1
242 activation [18]. As the early wound response developed, a notable reconfiguration in the Hippo pathway
243 dynamics became apparent. At 12 hpi, cells at the wound edge exhibited increased YAP1 nuclear staining,
244 coupled with an overall increase in TEAD1 (Fig 4J). This heightened activation indicated a responsive
245 modulation of the Hippo pathway, implicating it in the cellular and tissue growth regulation triggered by
246 the injury. The initial wound response also induced substantial alterations in cell phenotype, characterized
247 by the loss of epithelial markers (CK7 and albumin), disorganization of the cobblestone-like tissue
248 structure, and reorganization of the actin cytoskeleton (Fig 4N and 4O). Additionally, the emergence of
249 lamellipodia (Fig 3J, arrowed) indicated a shift toward a mesenchymal phenotype, suggestive of an EMT
250 process.

251 Twist1, a pivotal transcription factor associated with EMT initiation, displayed intense nuclear staining
252 within wound edge cells at 12 hpi, in stark contrast to its absence in control cells (Fig 3J). This observation
253 provided further substantiation for the occurrence of EMT during the initial phases of the wound response.

Proliferation burst, MET and Nanog/p16^{Ink4a} interplay resolution as the late wound response of WB-F344 cells.

At 24 hpi there starts a tremendous elevation of mitotic activity, which continues to grow at 40 hpi (Fig 3A), 4- and 5-fold increasing mitotic index, respectively, compared with control. The proportions of metaphases and anaphase+telophase phases at these time points were comparable with the control, approximately 1.1 - 1.3 (Fig 3C). In cell cycle histograms, at 24 hpi instead of one peak at 2C and another at 4C, we found a "ladder"- like histogram starting from G1, embracing a very bulk S-fraction fusing with G2 and extending up to the hyper-tetraploid fraction (Fig 3G). More conventional histogram was obtained at 40 hpi within the cells in the damaged area with peaks at 2C and 4C, however, some "ladder" remnants could be seen (Fig 3H); the polyploidy (mononuclear) level continued to increase from 24 hpi and was 1.5-fold higher in comparison with control, also octoploid and even bigger ploidy cells are already seen (Fig 3E-3H). Dropped to about 0.2% at 24 hpi (Fig 3D) the frequency of binuclear cells may indicate their attraction to the wound, followed by segregation and use in the wound healing process occurring before the burst of mitosis.

At the time of proliferation burst (24 and 40 hpi) WB-F344 cells regained epithelial phenotype (Fig 4O and 4P), no expression of Twist1 is present anymore (data not shown) and YAP1 and TEAD1 staining became less intense, suggesting Hippo pathway tumor suppressing function resuming (Fig 4K and 4L). Interestingly, we found that Oct4, one of the main stemness factors, while weakly stained with the monoclonal antibody (covering the 1st exon) in control WB-F344 cells (Fig 4G), and at 24 hpi show the non-specific antibody binding exclusively within morphologically distinct, distorted nuclei. The absence of the nuclear Oct4 staining in our model indicates the absence of the nuclear binding and hence the transactivating activity, in line with the absence of C-Myc activity in cell nuclei (Fig 4E and 4F) and may

276 also indicate to the restricted p53-controlled stemness potential of oval cells. The interplay between two
277 opposites for cell fate proteins, self-renewing Nanog or senescence-inducing $p16^{INK4A}$ continue to show
278 heterogeneous patterns (presuming oscillations) at 24 hpi at the wound edge started early after the injury
279 (Fig 4C), however, resolution comes at 40 hpi (almost full wound closure time) when Nanog over-
280 dominated and "casted-out" $p16^{Ink4a}$ from cell nuclei (Fig 4D). Previously rich in Nanog granules, cellular
281 cytoplasm is now clear from them, however, differently sized $p16^{Ink4a}$ positive cytoplasmic granules and
282 aggregates, approximately 1-3 per cell (if present) appeared (Fig 4D). It could be deduced, the "bistable
283 switch" between two toggles – stemness and senescence – in WB-F344 cells occurring along with wound
284 healing phases provides its positive outcome.

285 A summary of the observed cell changes during the whole wound healing process is provided in Table 2.

286 **Table 2. Summary of the observed events during the *in vitro* regeneration model.**

Cellular characteristics	Marker	Localization	Time points			
			Control	12hpi	24hpi	40hpi
Stemness	Nanog	Nucleus	+	++	++	+
		Cytoplasm	+/- few granules	++ granules	++ granules	+/-
Senescence	$P16^{Ink4a}$	Nucleus	+	++	++	-
		Cytoplasm	+ diffuse	++	++	+ granules
Bi-potential tissue-specific stemness potency	Albumin (hepatocyte)	++ diffuse	+/-	+/-	+	Albumin (hepatocyte)
	Cdk7 (cholangiocyte)	++	+/-	+/-	++	
Mobility EMT	Twist1		-	++	-	-
	Phenotype		Epithelial phenotype	EMT	EMT	MET
Hippo pathway	YAP1	Nucleus	+/-	+++	++	+

		Cytoplasm	+/-	-	-	-
	TEAD1	Nucleus	- peri-nuclear rings	+	+	+
		Cytoplasm	+	++	+	+

Outlined is the dynamic behavior of various cellular markers associated with key biological processes such as Stemness, Senescence, Bi-potential tissue-specific stemness potency, Mobility, and Hippo pathway over distinct time points post-injury (hpi) (12, 24, and 40 hours). Each row corresponds to a specific cellular characteristic, detailing the behavior of distinct markers and their localization within the cell. The markers exhibit diverse patterns of localization (nucleus, cytoplasm), intensity (+, ++, - or +/-) indicative of their presence or activity, and distinctive cellular behaviors (e.g., granules, diffuse, transition states like EMT and MET).

Discussion

Activation of the liver oval cells that contribute to liver regeneration is commonly observed in chronic or severe (acute) liver injury [19]. Diverse paracrine and autocrine signaling pathways have been described to control the LPC response [20]. However, it is far from being clear regarding the mechanisms that can be involved *in vivo* and *in vitro* systems for successful liver regeneration, especially in case of serious pathology. There is also an important concern about the therapy by LPCs in terms of its oncological safety. In the current study, we induced the massive injury, mechanically removing ~70% of the culture monolayer of rat liver oval cells. In general, two phases of cell response to injury ("priming" and "proliferation") were observed, which is in accord with the findings from *in vivo* models of partial hepatectomy [5]. Moreover, cell ploidy changes during the healing process including transient binucleation were also demonstrated, confirming the findings previously reported [13]. However, for the first time we were able to reveal and monitor the regulation of wound healing by the progenitor-driven

306 liver regeneration involving the recurrent nucleo-cytoplasmic transfer of two opposite regulators, Nanog
307 (stemness/cell-cycle progression) and p16^{Ink4a} (senescence/cell-cycle arrest). The upregulation of Nanog
308 at the priming stage (10-12 hp) was converted into Nanog secretion in the form of cytoplasmic and
309 extracellular Nanog-positive granules (vesicles) being outcompeted for the nuclear binding sites by
310 p16^{Ink4a} transferred into cell nuclei from cytoplasm. Both regulators are known to compete for the same
311 Cdk4/6 kinase of Cyclin D controlling the G1/S cell cycle checkpoint in stem cells: Nanog as an activator,
312 whereas p16^{Ink4a} as an inhibitor [21, 22]. Upon completion of cell proliferation at 40-48 h post-wounding,
313 the backward process is taking place: Nanog ousts p16^{Ink4a} from cell nucleus binding sites to cytoplasm,
314 suppressing the excited dual state of accelerated cell senescence, which was induced by the damage. Thus,
315 this system can be adapted to severe damage by employing a bistable switch of self-organization
316 (schematically shown in the Graphical abstract). At present, the concept of bistable switch-based
317 regulation is well-recognized and being intensively developed by Systems Biology as an example of
318 adaptive thermodynamics applicable to stem, differentiated and tumor cells [23-28]. In some previous
319 studies with breast tumor cells, there were possible fluctuations of cells with accelerated senescence
320 induced by drugs, e.g., between the Nanog- and p16-positive, including intermediate states [26, 29].
321 Moreover, the experiments with knockout mice showed that senescence, in particular, its p16^{Ink4a} regulator
322 is not only an antagonist of stemness but also is indispensable (along with secreted Il-6) to promote
323 reprogramming [30, 31]. Although usually this feature is solely ascribed to the senescence secretome, here
324 we demonstrate that the relationship between the potentially reprogramming Nanog and senescing p16^{Ink4a}
325 regulators is more complex with the involvement of nucleo-cytoplasmic relocation of these two opposites,
326 resulting in the negative feedback during second phase ending the healing process. The reprogramming
327 potential of the epithelial oval cells (WB-F344) used in this study was also displayed by EMT-MET
328 dynamics (as part of the same bistable switch), suggesting biphasic character of also this process. The

329 Hippo pathway, which is known to be associated with changes of cell fate and ploidy [32, 33], has been
330 also described in the context of liver regeneration and development [6]. We found the Hippo pathway
331 inactive in the near-confluent WB-F344 cell culture but it can be activated by turbulence (as judged by
332 perinuclear rings of TEAD1) and cytoplasmic-nuclear transition of activated YAP1 that coincides with
333 the priming phase and continues during replicative stress preceding and accompanying the boost of
334 proliferation at 24 h. The proliferation-associated "staircase" form of DNA histograms starting from the
335 early S-phase can be suggestive of the "staggering" of replication forks caused by transcription R-loops
336 [34]. This phenomenon is ascribed to hypertranscription activity of nuclear YAP1 that functions in
337 partnership with TEAD1 [35].

338 In fact, the WB-F344 line can be referred to as somatic oval cells possessing stem-like features, such as
339 an asymmetric cell division producing the progeny of different fates (differentiation and self-renewal).
340 Stem cells usually reside in quiescence and proliferate under stimuli [36]. However, cell-cycle regulation
341 of adult stem cells has not been explored as much as that of embryonic stem cells (ESCs). Most distinct
342 features of the cell-cycle of ESCs are as follows: non-functional G1/S-checkpoint, allowing rapid
343 proliferation, low functionality of the S-checkpoint, while the G2/M-checkpoints and spindle becomes
344 uncoupled from apoptosis [37, 38], favoring mitotic slippage into polyploidy.

345 In our model, DNA histograms of the near-confluent intact control showed most quiescent cells with low
346 mitotic index (MI) and insignificant degree of polyploidy (>4C). At the same time, there were cell-cycle
347 progression delay at 12 hpi with a halved mitotic index accompanied by disappearance of mononuclear
348 polyploid (>4-8C) cells and increasing of diploid (G0/G1) fraction with a negligible level of S-phase cells.
349 Notably, at 24 hpi there was a 5-fold but moderate elevation of polyploid fraction (>4C), not exceeding
350 8%. That means that the G1/S-checkpoint became adapted, thereby resulting in cell-cycle acceleration,
351 although S-phase was "staggering" at stalling replication forks due to collision between enforced

352 replication and hyper-transcription of active genes at the beginning of S-phase [39], which is suggestive
353 of replicative stress. In this situation, the "leakage" of the adapted G2/M-checkpoint with a lowered
354 threshold may reduce this stress, diverting a proportion of replicated cells from the mitotic cycle into
355 polyploidy (4C-8C). Our counts show a clear reciprocal relationship between the numbers of bi-nucleated
356 and mononucleated polyploid cells. One could suggest that those may be playing a role of the reservoir
357 for the emergent adaptation to wounding, thereby initially saving the energy needed for new DNA
358 synthesis. Therefore, it seems logical to hypothesize that only these types of cells (binucleated and
359 mononuclear polyploids) acquire the plasticity-assigned features of "avant-garde" undergoing EMT,
360 which is necessary for initial loose filling of the wound gap creating the stromal substrate for the upcoming
361 proliferation, simultaneously boosted by the Nanog-containing secretome. Once the aforementioned
362 priming response is completed and binucleate cell pool becomes exhausted, the energy of mitosis due to
363 the renewed DNA synthesis is directed to the formation of the next stock of polyploid cells (the
364 hypothetical Scheme of the ploidy response in oval cells using the binucleation/polyploidy (2C-4C-8C)
365 conveyor is presented in Fig 5.

366 **Fig 5. Hypothesis: Oval cells' ploidy circuit in wound healing.** (1) After the injury the fraction of
367 polyploid 8C cells undergoes reductive divisions resulting in 4C cells, which (2) immediately perform
368 cytokinesis-deficient karyokinesis producing binucleate cells. (3) 4C binucleate cells undergo postponed
369 reductive cytokinesis, producing 2C daughters moving into the wound gap as mesenchymal cells via EMT.
370 (4) In the wound gap, cells regain epithelial phenotype via MET and enter the mitotic cycle to replenish
371 the pool of 2C cells (5). However, a portion of cells via mitotic slippage (6) advance to the new polyploidy
372 cycle, restoring an exhausted pool of polyploid cells (7).

373 It is important to stress that this two-way process can be well organized by the negative feedback, thus
374 restricting the potential of uncontrolled growth that would let the "tumor genie out of the bottle". All

375 toggles observed here, such as Nanog/p16, EMT/MET, and presumably binucleation/polyploidization,
376 function here in a coordinated biphasic manner. While considering solid tumors as non-healing wounds
377 [40], our observations, on the other hand, suggest that just wound healing by oval cells with
378 reprogramming potential represents the barrier mechanisms against cancer. This barrier, consisting of
379 adaptive, biphasic, and completed self-organization, is functionally efficient based on cell-cycle
380 checkpoint regulation coupled to the nuclear-cytoplasmic shuttle of the opposite regulators. The transient
381 activation of Myc found in centrosomes and cytoplasm but not in cell nuclei suggests that likely N-Myc
382 with its cell migration-promoting role [41, 42] rather than nuclear C-Myc that maintains stress-dependent
383 polyploidy linked to cancer-initiating pathways [43, 44] is functionally predominant in oval cells, thereby
384 restricting tumor growth and uncontrolled polyploidization. Perhaps, that is why the WB-F433 cell line,
385 relatively resistant to ionizing irradiation [15, 45], is not tumorigenic *in vivo* [14]. Further research and
386 clinical trials are needed to use the oval cells with therapeutic purposes, offering hope for innovative and
387 effective treatments for liver pathologies including cancer.

388 Competing Interests

389 The author(s) declared no potential conflicts of interest with respect to the research, authorship, and/or
390 publication of this article.

391 Author Contributions

392 All authors have contributed to this article as follows:

393 Conceptualization, J.E. and M.L.; methodology, J.E., M.L. and K.S.; writing-original draft preparation,
394 M.L.; writing-review and editing, J.E., B.G.; project administration, D.P.; funding acquisition, D.P.;
395 supervision, J.E. All authors gave final approval for the manuscript.

References

1. Higgins G, Anderson G. Experimental pathology of the liver restoration of the liver of the white rat following partial surgical removal. Arch Pathol (Chic) 1931;12:186–202.
2. Devarbhavi H, Asrani SK, Arab JP, Nartey YA, Pose E, Kamath PS. Global burden of liver disease: 2023 update. J Hepatol. 2023;79(2):516-37.
3. Liu P, Mao Y, Xie Y, Wei J, Yao J. Stem cells for treatment of liver fibrosis/cirrhosis: clinical progress and therapeutic potential. Stem Cell Res Ther. 2022;13(1):356.
4. Grisham JW, Porta EA. Origin and Fate of Proliferated Hepatic Ductal Cells in the Rat: Electron Microscopic and Autoradiographic Studies. Exp Mol Pathol. 1964;3:242-61.
5. Fausto N. Liver regeneration. J Hepatol. 2000;32(1 Suppl):19-31.
6. Nguyen-Lefebvre AT, Selzner N, Wrana JL, Bhat M. The hippo pathway: A master regulator of liver metabolism, regeneration, and disease. FASEB J. 2021;35(5):e21570.
7. Pefani DE, O'Neill E. Hippo pathway and protection of genome stability in response to DNA damage. FEBS J. 2016;283(8):1392-403.
8. Zhang K, Zhang L, Liu W, Ma X, Cen J, Sun Z, et al. In Vitro Expansion of Primary Human Hepatocytes with Efficient Liver Repopulation Capacity. Cell Stem Cell. 2018;23(6):806-19 e4.
9. Matsumoto T. Implications of Polyploidy and Ploidy Alterations in Hepatocytes in Liver Injuries and Cancers. Int J Mol Sci. 2022;23(16).
10. Bird TG, Muller M, Boulter L, Vincent DF, Ridgway RA, Lopez-Guadamillas E, et al. TGFbeta inhibition restores a regenerative response in acute liver injury by suppressing paracrine senescence. Sci Transl Med. 2018;10(454).
11. Cheng N, Kim KH, Lau LF. Senescent hepatic stellate cells promote liver regeneration through IL-6 and ligands of CXCR2. JCI Insight. 2022;7(14).
12. Chembazhi UV, Bangru S, Hernaez M, Kalsotra A. Cellular plasticity balances the metabolic and proliferation dynamics of a regenerating liver. Genome Res. 2021;31(4):576-91.
13. Matsumoto T, Wakefield L, Tarlow BD, Grompe M. In Vivo Lineage Tracing of Polyploid Hepatocytes Reveals Extensive Proliferation during Liver Regeneration. Cell Stem Cell. 2020;26(1):34-47 e3.
14. Tsao MS, Smith JD, Nelson KG, Grisham JW. A diploid epithelial cell line from normal adult rat liver with phenotypic properties of 'oval' cells. Exp Cell Res. 1984;154(1):38-52.
15. Gerashchenko BI, Salmina K, Krigerts J, Erenpreisa J, Babsky AM. Induced Polyploidy and Sorting of Damaged DNA by Micronucleation in Radioresistant Rat Liver Epithelial Stem-Like Cells Exposed to X-Rays. Probl Radiac Med Radiobiol. 2019;24:220-34.
16. Erenpreisa J, Freivalds T. Anisotropic staining of apurinic acid with toluidine blue. Histochemistry. 1979;60(3):321-5.
17. Sugihara E, Kanai M, Matsui A, Onodera M, Schwab M, Miwa M. Enhanced expression of MYCN leads to centrosome hyperamplification after DNA damage in neuroblastoma cells. Oncogene. 2004;23(4):1005-9.
18. Franklin JM, Ghosh RP, Shi Q, Reddick MP, Liphardt JT. Concerted localization-resets precede YAP-dependent transcription. Nat Commun. 2020;11(1):4581.
19. Ma X, Qiu DK, Peng YS. Immunohistochemical study of hepatic oval cells in human chronic viral hepatitis. World J Gastroenterol. 2001;7(2):238-42.
20. Shu W, Yang M, Yang J, Lin S, Wei X, Xu X. Cellular crosstalk during liver regeneration: unity in diversity. Cell Commun Signal. 2022;20(1):117.

440 21. Zhang X, Neganova I, Przyborski S, Yang C, Cooke M, Atkinson SP, et al. A role for NANOG
441 in G1 to S transition in human embryonic stem cells through direct binding of CDK6 and CDC25A. J
442 Cell Biol. 2009;184(1):67-82.
443 22. Villacanas O, Perez JJ, Rubio-Martinez J. Structural analysis of the inhibition of Cdk4 and Cdk6
444 by p16(INK4a) through molecular dynamics simulations. J Biomol Struct Dyn. 2002;20(3):347-58.
445 23. Wolkenhauer O, Mesarovic M. Feedback dynamics and cell function: Why systems biology is
446 called Systems Biology. Mol Biosyst. 2005;1(1):14-6.
447 24. Wang L, Walker BL, Iannaccone S, Bhatt D, Kennedy PJ, Tse WT. Bistable switches control
448 memory and plasticity in cellular differentiation. Proc Natl Acad Sci U S A. 2009;106(16):6638-43.
449 25. Giuliani A, Bui TT, Helmy M, Selvarajoo K. Identifying toggle genes from transcriptome-wide
450 scatter: A new perspective for biological regulation. Genomics. 2022;114(1):215-28.
451 26. Erenpreisa J, Salmina K, Anatskaya O, Cragg MS. Paradoxes of cancer: Survival at the brink.
452 Semin Cancer Biol. 2022;81:119-31.
453 27. Noble R, Tasaki K, Noble PJ, Noble D. Biological Relativity Requires Circular Causality but
454 Not Symmetry of Causation: So, Where, What and When Are the Boundaries? Front Physiol.
455 2019;10:827.
456 28. Huang S, Ernberg I, Kauffman S. Cancer attractors: a systems view of tumors from a gene
457 network dynamics and developmental perspective. Semin Cell Dev Biol. 2009;20(7):869-76.
458 29. Gerashchenko BI, Salmina K, Eglitis J, Huna A, Grjunberga V, Erenpreisa J. Disentangling the
459 aneuploidy and senescence paradoxes: a study of triploid breast cancers non-responsive to neoadjuvant
460 therapy. Histochem Cell Biol. 2016;145(4):497-508.
461 30. Czarnecka-Herok J, Sliwinska MA, Herok M, Targonska A, Strzeszewska-Potyrala A, Bojko A,
462 et al. Therapy-Induced Senescent/Polyploid Cancer Cells Undergo Atypical Divisions Associated with
463 Altered Expression of Meiosis, Spermatogenesis and EMT Genes. Int J Mol Sci. 2022;23(15).
464 31. Mosteiro L, Pantoja C, de Martino A, Serrano M. Senescence promotes in vivo reprogramming
465 through p16(INK)(4a) and IL-6. Aging Cell. 2018;17(2).
466 32. Heng BC, Zhang X, Aubel D, Bai Y, Li X, Wei Y, et al. Role of YAP/TAZ in Cell Lineage Fate
467 Determination and Related Signaling Pathways. Front Cell Dev Biol. 2020;8:735.
468 33. Zhang S, Chen Q, Liu Q, Li Y, Sun X, Hong L, et al. Hippo Signaling Suppresses Cell Ploidy
469 and Tumorigenesis through Skp2. Cancer Cell. 2017;31(5):669-84 e7.
470 34. Allison DF, Wang GG. R-loops: formation, function, and relevance to cell stress. Cell Stress.
471 2019;3(2):38-46.
472 35. Lavado A, Park JY, Pare J, Finkelstein D, Pan H, Xu B, et al. The Hippo Pathway Prevents
473 YAP/TAZ-Driven Hypertranscription and Controls Neural Progenitor Number. Dev Cell.
474 2018;47(5):576-91 e8.
475 36. So WK, Cheung TH. Molecular Regulation of Cellular Quiescence: A Perspective from Adult
476 Stem Cells and Its Niches. Methods Mol Biol. 2018;1686:1-25.
477 37. Mantel C, Guo Y, Lee MR, Kim MK, Han MK, Shibayama H, et al. Checkpoint-apoptosis
478 uncoupling in human and mouse embryonic stem cells: a source of karyotpic instability. Blood.
479 2007;109(10):4518-27.
480 38. Neganova I, Lako M. G1 to S phase cell cycle transition in somatic and embryonic stem cells. J
481 Anat. 2008;213(1):30-44.
482 39. Maya-Mendoza A, Moudry P, Merchut-Maya JM, Lee M, Strauss R, Bartek J. High speed of
483 fork progression induces DNA replication stress and genomic instability. Nature. 2018;559(7713):279-
484 84.

485 40. Dvorak HF. Tumors: wounds that do not heal. Similarities between tumor stroma generation and
486 wound healing. N Engl J Med. 1986;315(26):1650-9.
487 41. Anderson S, Poudel KR, Roh-Johnson M, Brabletz T, Yu M, Borenstein-Auerbach N, et al.
488 MYC-nick promotes cell migration by inducing fascin expression and Cdc42 activation. Proc Natl Acad
489 Sci U S A. 2016;113(37):E5481-90.
490 42. Conacci-Sorrell M, Ngouenet C, Eisenman RN. Myc-nick: a cytoplasmic cleavage product of
491 Myc that promotes alpha-tubulin acetylation and cell differentiation. Cell. 2010;142(3):480-93.
492 43. Vazquez-Martin A, Anatskaya OV, Giuliani A, Erenpreisa J, Huang S, Salmina K, et al. Somatic
493 polyploidy is associated with the upregulation of c-MYC interacting genes and EMT-like signature.
494 Oncotarget. 2016;7(46):75235-60.
495 44. Anatskaya OV, Vinogradov AE. Polyploidy and Myc Proto-Oncogenes Promote Stress
496 Adaptation via Epigenetic Plasticity and Gene Regulatory Network Rewiring. Int J Mol Sci.
497 2022;23(17).
498 45. Gerashchenko BI, Azzam EI, Howell RW. Characterization of cell-cycle progression and growth
499 of WB-F344 normal rat liver epithelial cells following gamma-ray exposure. Cytometry A.
500 2004;61(2):134-41.

501

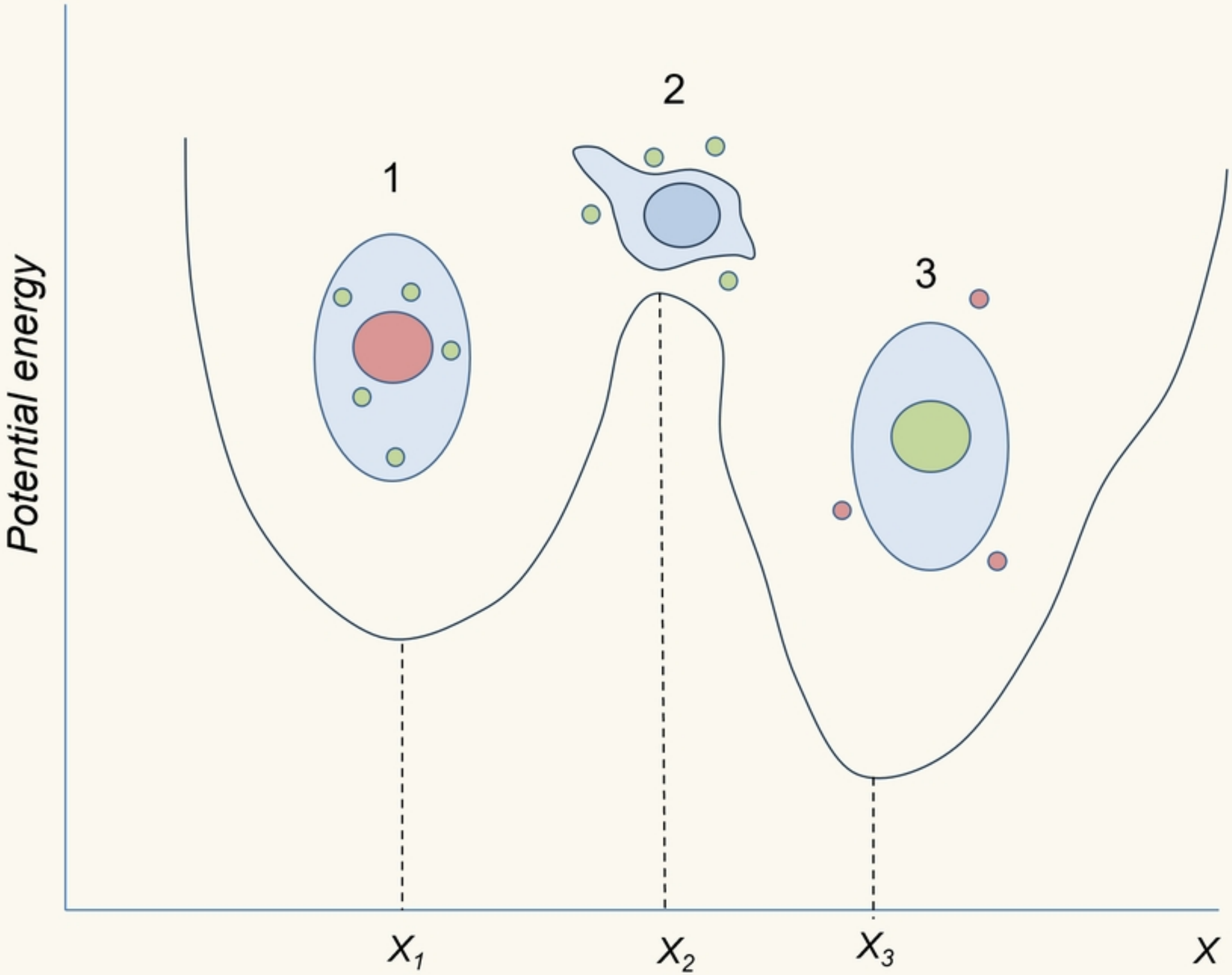

Figure1

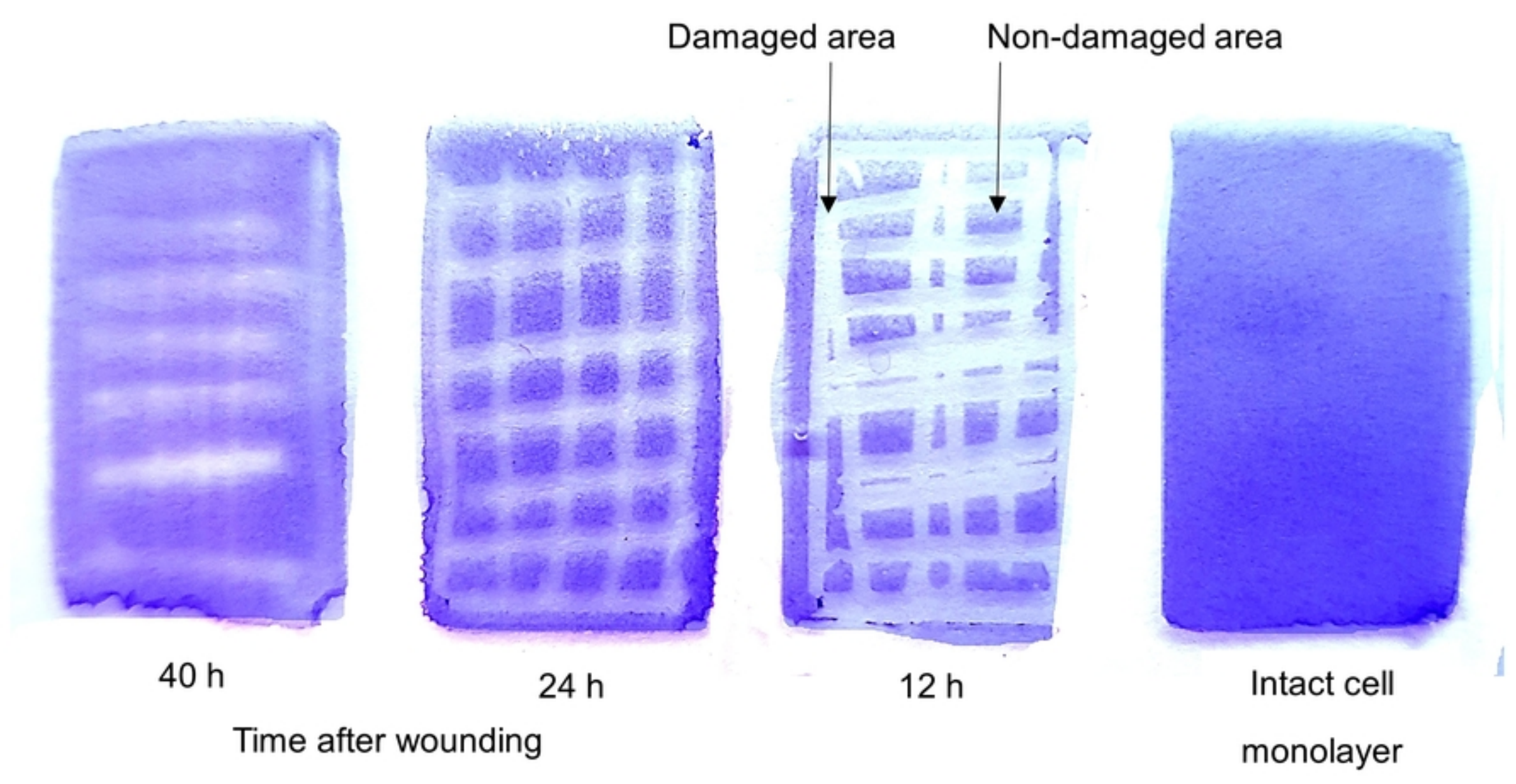
Damaged area
Non-damaged area
40 h
24 h
12 h
Intact cell
monolayer
Time after wounding

Figure2

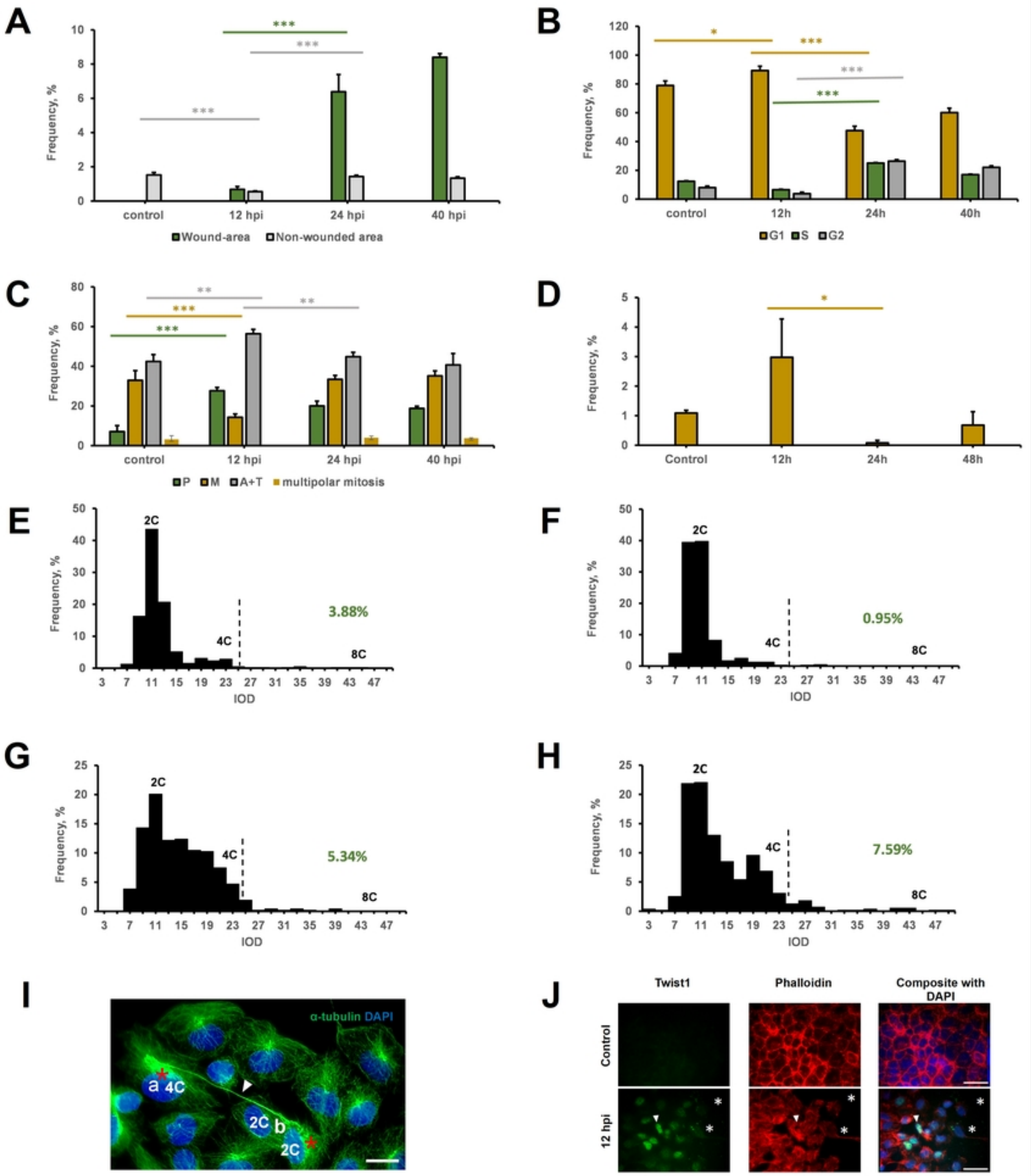
A
Frequency, %
control
12 hpi
24 hpi
40 hpi
Wound-area
Non-wounded area
B
Frequency, %
control
12h
24h
40h
G1
S
G2
C
Frequency, %
control
12 hpi
24 hpi
40 hpi
P
M
A+T
multipolar mitosis
D
Frequency, %
Control
12h
24h
48h
E
Frequency, %
2C
4C
8C
3.88%
IOD
F
Frequency, %
2C
4C
8C
0.95%
IOD
G
Frequency, %
2C
4C
8C
5.34%
IOD
H
Frequency, %
2C
4C
8C
7.59%
IOD
I
α-tubulin DAPI
a 4C
2C b
2C
J
Twist1
Phalloidin
Composite with DAPI
Control
12 hpi

Figure3

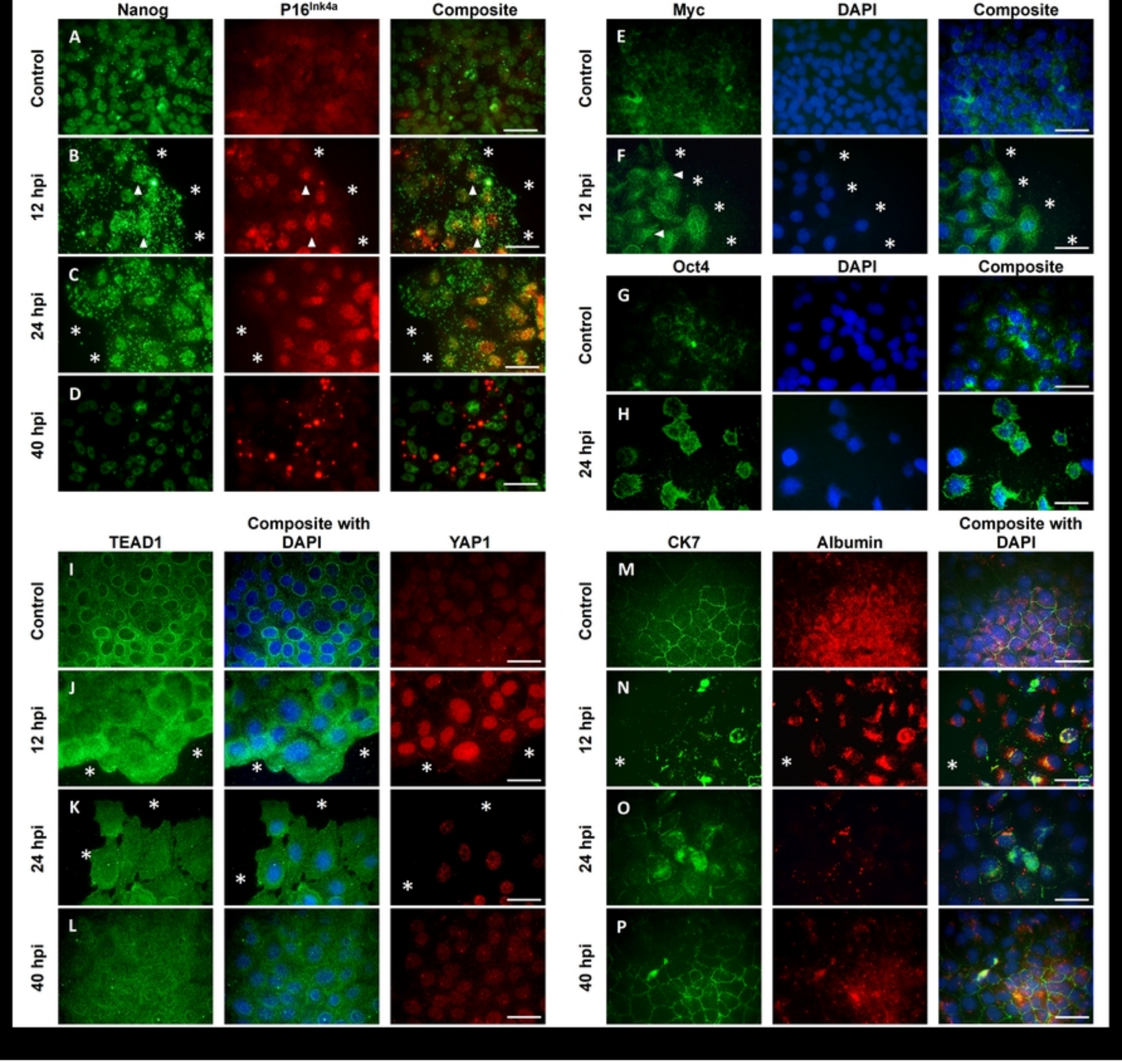
Nanog
P16Ink4a
Composite
Control
12 hpi
24 hpi
40 hpi
A
B
C
D
Myc
DAPI
Composite
E
F
Oct4
DAPI
Composite
G
H
TEAD1
Composite with DAPI
YAP1
I
J
K
L
CK7
Albumin
Composite with DAPI
M
N
O
P

Figure4

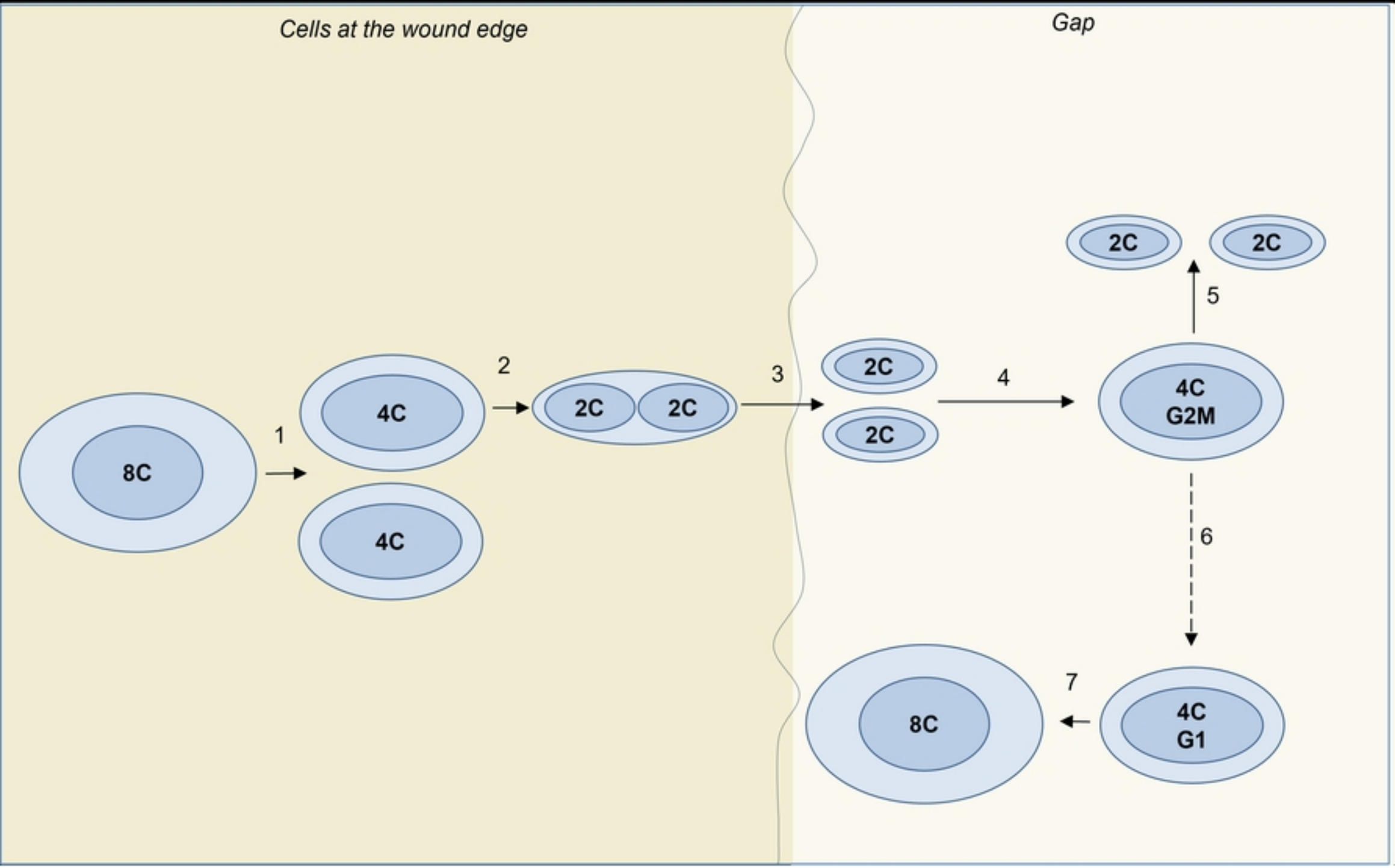
Cells at the wound edge
Gap
8C
1
4C
4C
2
2C
2C
3
2C
2C
4
4C
G2M
5
2C
2C
6
4C
G1
7
8C

Figure5